2021

Giant transport anisotropy in ReS2 revealed via nanoscale conducting path control

D. Li, S. Sun, Z. Xiao, J. Song, D.-F. Shao, E. Y. Tsymbal, S. Ducharme, and X. Hong

Giant Transport Anisotropy in ReS₂ Revealed via Nanoscale Conducting-Path Control

Dawei Li, Shuo Sun, Zhiyong Xiao, Jingfeng Song, Ding-Fu Shao, Evgeny Y. Tsymbal, Stephen Ducharme, and Xia Hong[*]

Department of Physics and Astronomy and Nebraska Center for Materials and Nanoscience,
University of Nebraska–Lincoln, Lincoln, Nebraska 68588-0299, USA

The low in-plane symmetry in layered 1T'-ReS₂ results in strong band anisotropy, while its manifestation in the electronic properties is challenging to resolve due to the lack of effective approaches for controlling the local current path. In this work, we reveal the giant transport anisotropy in monolayer to four-layer ReS₂ by creating directional conducting paths via nanoscale ferroelectric control. By reversing the polarization of a ferroelectric polymer top layer, we induce a conductivity switching ratio of $>1.5 \times 10^8$ in the ReS₂ channel at 300 K. Characterizing the domain-defined conducting nanowires in an insulating background shows that the conductivity ratio between the directions along and perpendicular to the Re chain can exceed 5.5×10^4 in monolayer ReS₂. Theoretical modeling points to the band origin of the transport anomaly and further reveals the emergence of a flat band in few-layer ReS₂. Our work paves the path for implementing highly anisotropic 2D materials for designing novel collective phenomena and electron lensing applications.

DOI: 10.1103/PhysRevLett.127.136803

Layered two-dimensional (2D) semiconductors such as black phosphorus and 1T'-rhenium disulfide (ReS₂) possess low in-plane symmetry, which leads to a rich spectrum of intriguing electronic and optical phenomena [1], including intrinsic band anisotropy [2], strongly anisotropic bound excitons and nonlinear optical responses [3–6], tunable hyperbolic plasmonics [7–9], large optical birefringence [10,11], moiré superlattices [12–14], and multiferroic behaviors [15,16]. The transition metal dichalcogenide (TMDC) ReS₂ is a direct band gap semiconductor, with the band gap (E_g) varying from 1.43 eV in monolayer samples to 1.35 eV in bulk [17]. It exhibits strong in-plane anisotropy between the directions along and perpendicular to the Re chains. Theoretical studies have shown that the band dispersions lead to highly direction-dependent mobility in ReS₂ [18,19], while direct mapping of its angle-resolved transport remains challenging due to the lack of effective strategies to control the local current path [20,21].

A promising approach to define reconfigurable, directional conduction paths in 2D semiconductors is to leverage the nanoscale controllable polarization of an adjacent ferroelectric layer. In previous studies, ferroelectric domain patterning has been exploited to impose a wide range of functionalities in TMDCs [22,23], including programmable homo- and heterojunction states [24,25] and photovoltaic effects [26], nanoscale excitonic modulation [27,28], and nonlinear optical filtering [29]. Combining local polarization writing with the ferroelectric field effect enables the programming of nanoscale conduction paths within an insulating background, which can confine the local current flow in different predesigned directions on the same sample. Unlike lithographically defined nanowires, the nonvolatile field effect approach is clean and reversible and does not involve uncontrollable sample-to-sample variations.

In this work, we exploited nanoscale polarization control of a ferroelectric copolymer poly(vinylidene fluoride-trifluoroethylene) [P(VDF-TrFE)] top layer to probe the transport anisotropy in atomically thin ReS₂. By characterizing the domain-defined conducting nanowires in the insulating channel [Fig. 1(a)], we mapped out the angle-resolved conductance of single-layer (1L), bilayer (2L), and four-layer (4L) ReS₂ field effect transistors (FETs), which revealed a giant conductivity ratio of 5.5×10^4 between the directions along and perpendicular to the Re chain [Fig. 1(b)]. The transport results can be well accounted for by the band anisotropy in conjunction with the electron-phonon scattering, as revealed by our first-principles density functional theory (DFT) modeling, which further points to the emergence of a flat band in the 4L ReS₂. Our study illustrates a powerful approach for resolving nanoscale electronic signatures of emergent band properties in van der Waals (vdW) materials, as well as presenting a promising material platform for realizing correlation-driven quantum phenomena and electron lensing applications.

We mechanically exfoliated monolayer and few-layer ReS₂ flakes from bulk single crystals onto gel films. The layer number was confirmed by atomic force microscopy (AFM, Bruker MultiMode 8) studies combined with the

Raman frequency difference Δ between modes I and III. The crystalline orientation of ReS$_2$ was identified by angle-resolved parallel-polarized Raman scattering measurements (see Supplemental Material) [30,31]. Selected 1–4L ReS$_2$ flakes were transferred onto SiO$_2$ (290 nm)/doped Si substrates prepatterned with Cr/Au (2 nm/10 nm) electrodes, forming FET devices. Next, we deposited nine monolayers of P(VDF-TrFE) film on top of ReS$_2$ using the Langmuir-Blodgett (LB) technique [32] followed by a thermal annealing treatment at 135 °C for 80 min (see Supplemental Material) [30]. Our previous studies have shown that the thermally treated P(VDF-TrFE) on ReS$_2$ forms close-packed single crystalline nanowires with the polar axis along the film normal [33]. To switch the ferroelectric polarization, a ± 11 V dc bias (V_{bias}) was applied to a conductive PtIr-coated tip (Bruker SCM-PIC-V2), with domain writing controlled by the NanoMan program. The resulting domain structures were imaged using piezoresponse force microscopy (PFM). The electrical characterization was performed using the semiconductor parameter analyzer (Keysight B1500A) after domain patterning, while the sample was kept in the AFM during the entire process.

Figures 1(c)–1(e) display the PFM phase images taken on a 1L ReS$_2$ FET, with the P(VDF-TrFE) top layer in the as-prepared, no-poling state [Fig. 1(c)] and the uniformly patterned polarization down (P_{down}) [Fig. 1(d)] and up (P_{up}) [Fig. 1(e)] states, respectively. In all states, the sample exhibits a linear source-drain current-voltage ($I_d - V_d$) relation, confirming the Ohmic characteristic (see Supplemental Fig. S3) [30]. Figure 1(f) compares the I_d versus back-gate voltage (V_{bg}) relation for these three states, showing that the P_{down} (P_{up}) state accumulates (depletes) electrons in ReS$_2$, as expected. The transfer curve in the P_{up} state exhibits a hole-doped characteristic, with I_d decreasing with increasing V_{bg}. In contrast, the P_{down} polarization of P(VDF-TrFE) introduces a high level of electron doping in ReS$_2$, changing the dominant carrier type from p type to n type. In this state, the ReS$_2$ channel remains highly conductive over the entire V_{bg} range, showing that the accumulated electron density well exceeds what can be effectively depleted by the SiO$_2$ back gate. The current switching ratio between the P_{down} and P_{up} states reaches 5.3×10^6 at $V_{\text{bg}} = 7$ V. A higher switching ratio may be expected at $+7 \text{ V} \leq V_{\text{bg}} \leq +40$ V, where the 1L ReS$_2$ becomes so insulating in the P_{up} state that the current level is below the instrument resolution.

We also achieved nonvolatile current modulation in the 2L and 4L ReS$_2$ FET devices [Fig. 1(g) and Supplemental Fig. S3] [30]. In the 4L device, we extracted from the transfer curves a high current switching ratio of 1.5×10^8 at $V_{\text{bg}} = 12$ V, which is among the highest values reported in ferroelectric-gated 2D FETs [34]. Compared with the polymorphous polymer films prepared via spin coating
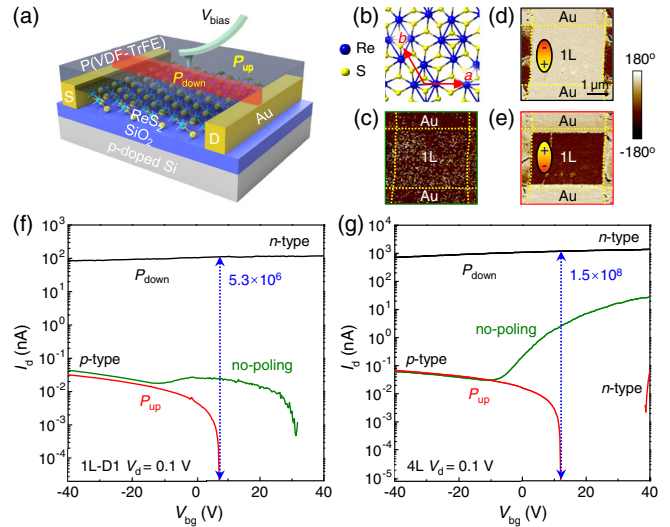

FIG. 1. (a) Device schematic. (b) Schematic crystal structure of ReS$_2$. (c)–(e) PFM phase images of a 1L ReS$_2$ FET (1L-D1) with the P(VDF-TrFE) top gate (c) in the initial no-poling state and uniformly polarized in the (d) P_{down} and (e) P_{up} states. (f) I_d versus V_{bg} for the 1L ReS$_2$ FET in (c)–(e) in the P_{down}, P_{up}, and no-poling states of P(VDF-TrFE). (g) I_d versus V_{bg} for a 4L ReS$_2$ in different polar states of P(VDF-TrFE).

[21], where the net polarization is compromised due to the randomly oriented polar grains, the thermally treated LB films enable the remarkable level of doping modulation, which is critical for defining a highly insulating background. In the P_{up} state, both 2L and 4L channels exhibit a transition from p-type to n-type transfer characteristics with increasing V_{bg}, indicating that the Fermi level is shifted close to the conduction band. Even though the fractional change of the doping level is expected to increase with decreasing channel thickness, we find that the ferroelectric field effect is larger in the thicker samples. A likely reason is that 1L ReS$_2$ is highly insulating in the P_{up} state and cannot provide sufficient screening to P(VDF-TrFE). This results in a high depolarization field, which leads to incomplete polarization switching [23].

To create a directional conducting nanowire, we switched the polarization of P(VDF-TrFE) into the uniform P_{up} state, setting the entire ReS$_2$ channel in a highly insulating state, and then wrote a line-shaped P_{down} domain between the source and drain. Given the high current switching ratio, the nanowire conductance remains orders of magnitude higher than the insulating background over the entire V_{bg} range. We worked with P_{down} nanowires that are 300–400 nm wide. At this width range, electron conduction can be effectively confined to be along the nanowire direction, while the nanowire can sustain the 2D transport characteristic without a prominent edge contribution. Writing P_{down} nanowire domains along different orientations, thus, enables angle-resolved conductance measurements on the same sample. Figure 2 shows
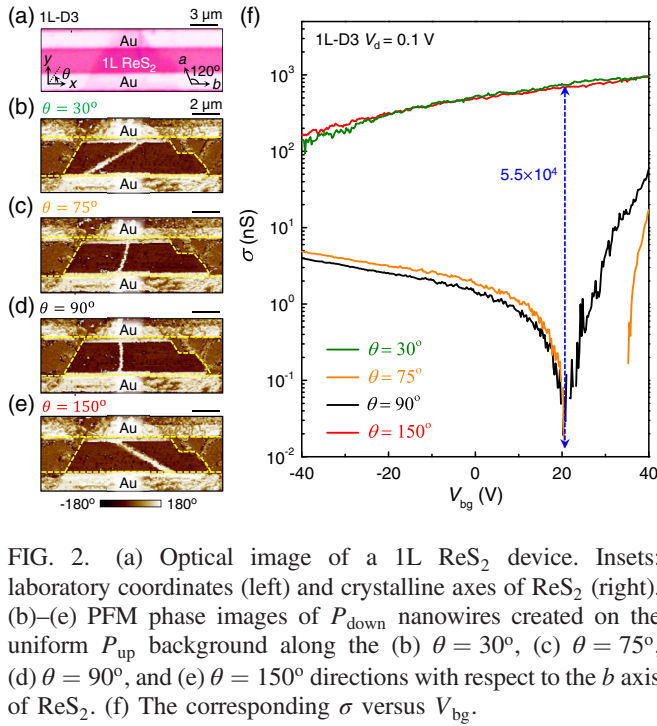
FIG. 2. (a) Optical image of a 1L ReS$_2$ device. Insets: laboratory coordinates (left) and crystalline axes of ReS$_2$ (right). (b)–(e) PFM phase images of P_{down} nanowires created on the uniform P_{up} background along the (b) $\theta = 30^o$, (c) $\theta = 75^o$, (d) $\theta = 90^o$, and (e) $\theta = 150^o$ directions with respect to the b axis of ReS$_2$. (f) The corresponding σ versus V_{bg}.

the results obtained on a 1L ReS$_2$ FET using this approach. The b axis of this sample is perpendicular to the channel orientation [Fig. 2(a)] [30]. We wrote a series of P_{down} nanowires connecting the source and drain electrodes [Figs. 2(b)–2(e)]. Figure 2(f) shows the corresponding channel sheet conductance $\sigma = (L/W)(I_d/V_d)$, or 2D conductivity, as a function of V_{bg} for the nanowires. Here, L and W are the length and width of the nanowire, respectively, and the angle θ is defined with respect to the b axis of ReS$_2$. It is evident that there are two distinct transfer characteristics for these four angles. For the nanowire along the directions of $\theta = 30^o$ and 150°, which are oriented close to the b axis, the channel remains highly conductive with n-type characteristic over the entire V_{bg} range. In contrast, for $\theta = 75^o$ and 90°, which are close to the direction perpendicular to the b axis, the ReS$_2$ nanowires exhibit very low conductance, with the channel effectively turned into p type at $V_{bg} < 20$ V. At $V_{bg} = 20$ V, ReS$_2$ exhibits up to 5.5×10^4-fold change in conductance between the directions of $\theta = 30^o$ and $\theta = 75^o$, which also corresponds to a change of carrier type from electron- to hole-doped behavior. An even larger transport anisotropy is expected between $V_{bg} = 20$ and 35 V, where the channel is too insulating along the $\theta = 75^o$ direction to be measured.

To map out the angle-resolved transport close to the conduction band edge, we extracted the conductivity of nanowires in various directions at fixed V_{bg}. We chose a V_{bg} at which the sample is at the threshold of being turned on and electron doped in all directions. Figure 3(a) shows the polar plot of σ for the 1L ReS$_2$ sample at $V_{bg} = 40$ V.

The sheet conductance measured at the angles $\theta = 30^o$ (954 nS) is about 56 times of that at $\theta = 105^o$ (17 nS). Similar electron conduction anisotropy has been observed in the 2L [Fig. 3(b)] and 4L [Fig. 3(c)] ReS$_2$ samples (see Supplemental Material) [30]. Despite the fluctuation of the data points, which can be affected by the local defects in the P(VDF-TrFE) top layer close to the nanowire area, all samples exhibit high conductance in the vicinity of the b axis ($\theta = 0°$) and low conductance when θ approaches 90°. The anisotropy is strongly enhanced in the few-layer sample, with a giant anisotropic conductance ratio of about 1.7×10^3 observed in the 4L ReS$_2$ device between the directions of $\theta = 0°$ (496.5 nS) and 120° (0.3 nS) [Fig. 3(c)]. Unlike the modulation observed in Fig. 2(f), this change does not involve the change of carrier type, thus reflecting solely the electron transport anisotropy. Note that the observed angular dependence of σ reflects a lack of mirror symmetry with respect to the $\theta = 0°$ axis. As 1T'-ReS$_2$ belongs to the space group $P\bar{1}$, it has only an inversion symmetry.

The conductance in ReS$_2$ is determined by the electron mobility $\mu = e\tau/m^*$, where e is the electron charge, τ is the average scattering time induced by defects, impurities, or phonons, and m^* is the effective mass determined by the band structure $E(\mathbf{k})$ as $m^* = \hbar^2/[\partial^2 E(\mathbf{k})/\partial\mathbf{k}^2]$. To understand the role of band dispersion on the anisotropic conduction, we performed the first-principles DFT
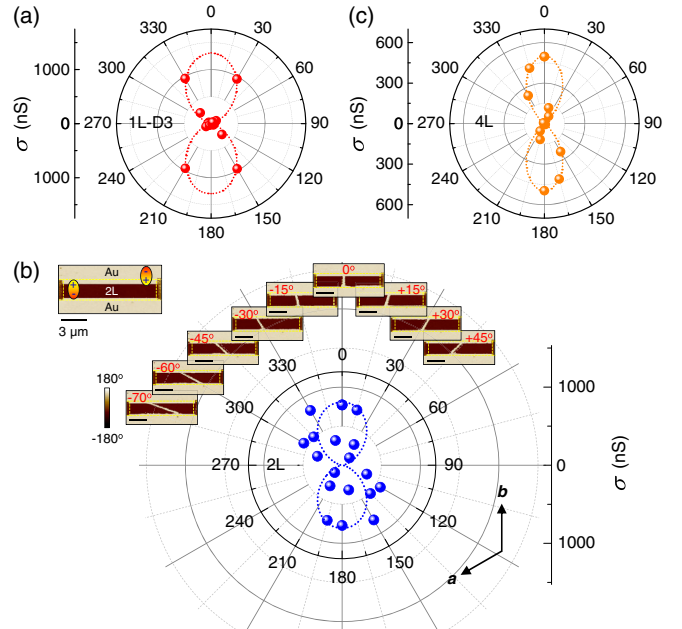

FIG. 3. Polar plots of σ of (a) a 1L ReS$_2$ at $V_{bg} = 40$ V, (b) a 2L ReS$_2$ at $V_{bg} = -40$ V, and (c) a 4L ReS$_2$ at $V_{bg} = 10$ V. The dashed lines serve as a guide to the eye. Insets in (b): PFM phase images of the corresponding P_{down} nanowires. The top left image corresponds to the initial uniform P_{up} domain before the nanowire patterning. All scale bars are 3 μm.

calculations for the band structures of 1L [Fig. 4(a)], 2L [Fig. 4(b)], and 4L [Fig. 4(c)] ReS$_2$. The details of the calculation can be found in Supplemental Material [30,35–38]. The result obtained for 1L ReS$_2$ is consistent with the previous report [20]. For all three layer numbers, the band dispersion along the k_x direction (b axis) at the conduction band minimum (CBM) exhibits a larger curvature compared with that along the k_y direction [Figs. 4(d)–4(f)], yielding a lighter m^* along the b axis ($\theta = 0°$) and a heavier m^* perpendicular to the b axis ($\theta = 90°$). The anisotropy of the band dispersion, on the other hand, is significantly enhanced with increasing layer thickness of ReS$_2$. For all layer thicknesses, the inversion symmetry of the space group $P\bar{1}$ has been preserved in the calculated m^* (see Supplemental Material) [30].

Figures 4(g)–4(i) show the normalized $1/m^*$ versus θ relation superimposed onto the normalized conductance (σ_{norm}) data. For 1L ReS$_2$, $1/m^*$ shows a similar θ dependence as the measured σ, i.e., the maximum values appear at orientations close to $\theta = 0°$ and $180°$, and the minimum values appear close to the $\theta = 90°$ and $270°$ directions [Fig. 4(g)]. The variation in $1/m^*$, however, cannot fully account for the relative change in σ_{norm}. Considering that the band anisotropy also affects the election-phonon scattering, we incorporated the contribution of phonon scattering in mobility μ by using the Takagi formula [39–41]:

$$\mu_i = \frac{e\hbar^3 C_i}{k_B T m_i^* m_d^* D_i^2}. \qquad (1)$$

Here, i refers to the conduction direction, and $m_d^* = \sqrt{m_x^* m_y^*}$ is the density-of-state effective mass for an anisotropic electronic band. The deformation potential constant is defined as $D_i = \partial E_V / \partial \varepsilon_i$, where E_V is the energy of the CBM and ε_i is a strain applied along direction i. The 2D elastic modulus along the conduction direction is calculated using $C_i = 2\partial^2 E_{\mathrm{total}}/S_0 \partial \varepsilon_1^2$, where E_{total} is the total energy of ReS$_2$ and S_0 is the area of the 2D ReS$_2$ without strain. As shown in Fig. 4(g), the modeled μ versus θ relation shows improved agreement with $\sigma_{\mathrm{norm}}(\theta)$, indicating that the anisotropic conductance in 1L ReS$_2$ is resulted from the convoluted effects of the anisotropic band dispersion and the phonon scattering. On the other hand, we find that $\sigma_{\mathrm{norm}}(\theta)$ for the 2L [Fig. 4(h)] and 4L [Fig. 4(i)] ReS$_2$ can be well explained by the calculated $1/m^*$ versus θ relation. This is because the anisotropy of the conduction band dispersion is significantly enhanced in thicker ReS$_2$ [Figs. 4(d)–4(f)], so that the angular dependence of electron-phonon scattering plays a relatively minor role in the electron transport in 2L and 4L ReS$_2$.

These findings are in sharp contrast with the previous studies of directional transport in ReS$_2$ using a circular sample geometry with multiple point contacts along various
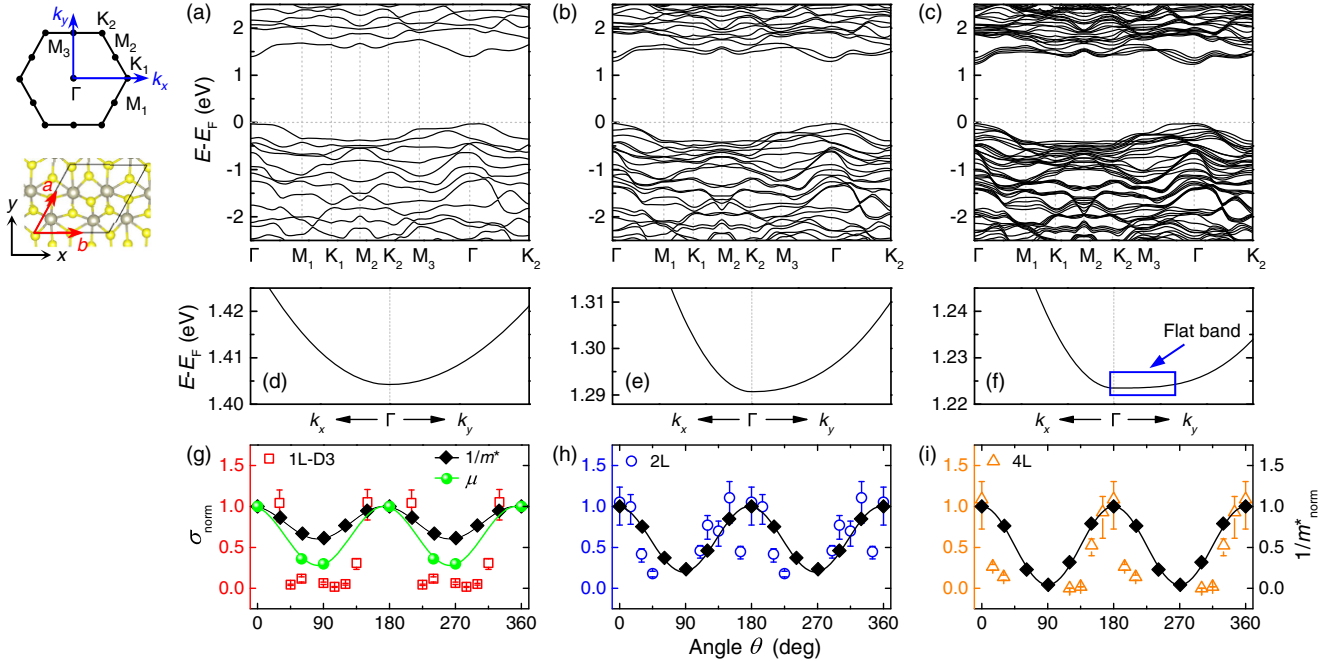

FIG. 4. (a)–(c) Band structures of (a) 1L, (b) 2L, and (c) 4L ReS$_2$. Insets in (a) show the symmetry points in the first Brillouin zone (top), where k_x and k_y are the same as x and y directions in the real space unit cell (bottom), with (d)–(f) the corresponding expanded views near the Γ point. (g) σ_{norm} versus θ (open symbols) for the 1L ReS$_2$ in Fig. 3(a) superimposed with the normalized $1/m^*_{\mathrm{norm}}$ and μ_{norm} (solid symbols). (h),(i) σ_{norm} versus θ (open symbols) for (h) the 2L ReS$_2$ in Fig. 3(b) and (i) 4L ReS$_2$ in Fig. 3(c) superimposed with $1/m^*_{\mathrm{norm}}$ (solid symbols).

directions [20] or micron-sized conduction channels [21], where the experimentally extracted anisotropic conductance ratio is significantly smaller than the theoretical prediction. In both approaches, the local current path within the sample cannot be well controlled. The measurements, thus, collect current flows over a wide range of angle distributions, making it challenging to quantitatively analyze the directional conduction.

What is intriguing is the emergence of a nearly flat band in 4L ReS$_2$ at the CBM along the k_y direction [Fig. 4(f)], leading to a drastic increase in m^* for $\theta = 90°$ (see Supplemental Material), which can well account for the giant electron transport anisotropy observed in 4L ReS$_2$ [30]. Such band dispersion highly resembles what is predicted for one-dimensional graphene superlattices (GSLs) [42]. It is thus conceivable to design ReS$_2$-based novel electron lensing applications by either varying the layer numbers along the conducting path through assembling artificial ReS$_2$ heterostructures or integrating few-layer ReS$_2$ with other isotropic vdW materials. Compared with the GSL approach, which is challenging to realize due to difficulties in imposing a nanoscale 1D periodic potential, few-layer ReS$_2$-based electron supercollimation builds upon the fabrication of vdW heterostructures and is free of lithography-induced disorder and fluctuation. The flat band and the associated heavy effective mass also make few-layer ReS$_2$ a promising platform for hosting collective phenomena, such as magnetism and superconductivity.

In summary, we have resolved for the first time the giant transport anisotropy in mono- to few-layer ReS$_2$ by creating directional conducing paths through the nanoscale ferroelectric control, which reveals a 2D conductivity ratio exceeding 5.5×10^4 between the directions along and perpendicular to the b axis in 1L ReS$_2$. Our DFT calculations point to the band origin of this intriguing behavior and reveal the emergence of a flat band in few-layer ReS$_2$. Our approach can be widely applied to other anisotropic vdW materials, providing a novel route for resolving nanoscale electronic signatures of emergent band properties and designing collective phenomena and electron lensing applications in vdW heterostructures.

*Corresponding author.
xia.hong@unl.edu

[1] S. Barraza-Lopez, F. Xia, W. Zhu, and H. Wang, Beyond graphene: Low-symmetry and anisotropic 2D materials, J. Appl. Phys. **128**, 140401 (2020).

[2] C. Gong, Y. Zhang, W. Chen, J. Chu, T. Lei, J. Pu, L. Dai, C. Wu, Y. Cheng, T. Zhai, L. Li, and J. Xiong, Electronic and optoelectronic applications based on 2D novel anisotropic transition metal dichalcogenides, Adv. Sci. **4**, 1700231 (2017).

[3] X. Wang, A. M. Jones, K. L. Seyler, V. Tran, Y. Jia, H. Zhao, H. Wang, L. Yang, X. Xu, and F. Xia, Highly anisotropic and robust excitons in monolayer black phosphorus, Nat. Nanotechnol. **10**, 517 (2015).

[4] X. Meng, Y. Zhou, K. Chen, R. H. Roberts, W. Wu, J. F. Lin, R. T. Chen, X. Xu, and Y. Wang, Anisotropic saturable and excited-state absorption in bulk ReS$_2$, Adv. Opt. Mater. **6**, 1800137 (2018).

[5] Q. Cui, R. A. Muniz, J. Sipe, and H. Zhao, Strong and anisotropic third-harmonic generation in monolayer and multilayer ReS$_2$, Phys. Rev. B **95**, 165406 (2017).

[6] D. Li, C. Wei, J. Song, X. Huang, F. Wang, K. Liu, W. Xiong, X. Hong, B. Cui, and A. Feng, Anisotropic enhancement of second-harmonic generation in monolayer and bilayer MoS$_2$ by integrating with TiO$_2$ nanowires, Nano Lett. **19**, 4195 (2019).

[7] A. Nemilentsau, T. Low, and G. Hanson, Anisotropic 2D Materials for Tunable Hyperbolic Plasmonics, Phys. Rev. Lett. **116**, 066804 (2016).

[8] C. Wang, G. Zhang, S. Huang, Y. Xie, and H. Yan, The optical properties and plasmonics of anisotropic 2D materials, Adv. Opt. Mater. **8**, 1900996 (2020).

[9] T. Low, A. Chaves, J. D. Caldwell, A. Kumar, N. X. Fang, P. Avouris, T. F. Heinz, F. Guinea, L. Martin-Moreno, and F. Koppens, Polaritons in layered two-dimensional materials, Nat. Mater. **16**, 182 (2017).

[10] H. Yang, H. Jussila, A. Autere, H.-P. Komsa, G. Ye, X. Chen, T. Hasan, and Z. Sun, Optical waveplates based on birefringence of anisotropic two-dimensional layered materials, ACS Photonics **4**, 3023 (2017).

[11] N. Papadopoulos, R. Frisenda, R. Biele, E. Flores, J. R. Ares, C. Sánchez, H. S. J. van der Zant, I. J. Ferrer, R. D'Agosta, and A. Castellanos-Gomez, Large birefringence and linear dichroism in TiS$_3$ nanosheets, Nanoscale **10**, 12424 (2018).

[12] Z. Qiu, M. Trushin, H. Fang, I. Verzhbitskiy, S. Gao, E. Laksono, M. Yang, P. Lyu, J. Li, J. Su, M. Telychko, K. Watanabe, T. Taniguchi, J. Wu, A. H. C. Neto, L. Yang, G. Eda, S. Adam, and J. Lu, Giant gate-tunable bandgap renormalization and excitonic effects in a 2D semiconductor, Sci. Adv. **5**, eaaw2347 (2019).

[13] Y. Liu, J. N. B. Rodrigues, Y. Z. Luo, L. Li, A. Carvalho, M. Yang, E. Laksono, J. Lu, Y. Bao, H. Xu, S. J. R. Tan, Z. Qiu,

C. H. Sow, Y. P. Feng, A. H. C. Neto, S. Adam, J. Lu, and K. P. Loh, Tailoring sample-wide pseudo-magnetic fields on a graphene–black phosphorus heterostructure, Nat. Nanotechnol. **13**, 828 (2018).

[14] R. Plumadore, M. M. Al Ezzi, S. Adam, and A. Luican-Mayer, Moiré patterns in graphene–rhenium disulfide vertical heterostructures, J. Appl. Phys. **128**, 044303 (2020).

[15] S. Barraza-Lopez, B. M. Fregoso, J. W. Villanova, S. S. Parkin, and K. Chang, Colloquium: Physical properties of group-IV monochalcogenide monolayers, Rev. Mod. Phys. **93**, 011001 (2021).

[16] F. Xia, H. Wang, J. C. M. Hwang, A. H. C. Neto, and L. Yang, Black phosphorus and its isoelectronic materials, Nat. Rev. Phys. **1**, 306 (2019).

[17] S. Tongay, H. Sahin, C. Ko, A. Luce, W. Fan, K. Liu, J. Zhou, Y.-S. Huang, C.-H. Ho, J. Yan, D. F. Ogletree, S. Aloni, J. Ji, S. Li, J. Li, F. M. Peeters, and J. Wu, Monolayer behaviour in bulk ReS_2 due to electronic and vibrational decoupling, Nat. Commun. **5**, 3252 (2014).

[18] J. L. Webb, L. S. Hart, D. Wolverson, C. Chen, J. Avila, and M. C. Asensio, Electronic band structure of ReS_2 by high-resolution angle-resolved photoemission spectroscopy, Phys. Rev. B **96**, 115205 (2017).

[19] B. S. Kim, W. Kyung, J. Denlinger, C. Kim, and S. Park, Strong one-dimensional characteristics of hole-carriers in ReS_2 and $ReSe_2$, Sci. Rep. **9**, 2730 (2019).

[20] E. Liu, Y. Fu, Y. Wang, Y. Feng, H. Liu, X. Wan, W. Zhou, B. Wang, L. Shao, and C.-H. Ho, Integrated digital inverters based on two-dimensional anisotropic ReS_2 field-effect transistors, Nat. Commun. **6**, 6991 (2015).

[21] R. Wang, F. Zhou, L. Lv, S. Zhou, Y. Yu, F. Zhuge, H. Li, L. Gan, and T. Zhai, Modulation of the anisotropic electronic properties in ReS_2 via ferroelectric film, CCS Chem. **1**, 268 (2019).

[22] X. Hong, Emerging ferroelectric transistors with nanoscale channel materials: the possibilities, the limitations, J. Phys. Condens. Matter **28**, 103003 (2016).

[23] H. Ryu, K. Xu, D. Li, X. Hong, and W. Zhu, Empowering 2D nanoelectronics via ferroelectricity, Appl. Phys. Lett. **117**, 080503 (2020).

[24] Z. Xiao, J. Song, D. K. Ferry, S. Ducharme, and X. Hong, Ferroelectric-Domain-Patterning-Controlled Schottky Junction State in Monolayer MoS_2, Phys. Rev. Lett. **118**, 236801 (2017).

[25] G. Wu, B. Tian, L. Liu, W. Lv, S. Wu, X. Wang, Y. Chen, J. Li, Z. Wang, S. Wu, H. Shen, T. Lin, P. Zhou, Q. Liu, C. Duan, S. Zhang, X. Meng, S. Wu, W. Hu, X. Wang, J. Chu, and J. Wang, Programmable transition metal dichalcogenide homojunctions controlled by nonvolatile ferroelectric domains, Nat. Electron. Rev. **3**, 43 (2020).

[26] L. Lv, F. Zhuge, F. Xie, X. Xiong, Q. Zhang, N. Zhang, Y. Huang, and T. Zhai, Reconfigurable two-dimensional optoelectronic devices enabled by local ferroelectric polarization, Nat. Commun. **10**, 3331 (2019).

[27] C. H. Li, K. M. McCreary, and B. T. Jonker, Spatial control of photoluminescence at room temperature by ferroelectric domains in monolayer WS_2/PZT hybrid structures, ACS Omega **1**, 1075 (2016).

[28] B. Wen, Y. Zhu, D. Yudistira, A. Boes, L. Zhang, T. Yidirim, B. Liu, H. Yan, X. Sun, and Y. Zhou, Ferroelectric-driven exciton and trion modulation in monolayer molybdenum and tungsten diselenides, ACS Nano **13**, 5335 (2019).

[29] D. Li, X. Huang, Z. Xiao, H. Chen, L. Zhang, Y. Hao, J. Song, D.-F. Shao, E. Y. Tsymbal, Y. Lu, and X. Hong, Polar coupling enabled nonlinear optical filtering at MoS_2/ferroelectric heterointerfaces, Nat. Commun. **11**, 1422 (2020).

[30] See Supplemental Material at http://link.aps.org/supplemental/10.1103/PhysRevLett.127.136803 for the details of sample characterization, electrical measurements, and theoretical calculations.

[31] D. A. Chenet, O. B. Aslan, P. Y. Huang, C. Fan, A. M. van der Zande, T. F. Heinz, and J. C. Hone, In-plane anisotropy in mono- and few-layer ReS_2 probed by Raman spectroscopy and scanning transmission electron microscopy, Nano Lett. **15**, 5667 (2015).

[32] S. Ducharme, S. P. Palto, V. M. Freidkin, and L. M. Blinov, *Ferroelectric Polymer Langmuir-Blodgett Films* (Academic Press, San Diego, 2002), Vol. 3.

[33] D. Li, S. Sun, K. Wang, Z. Ahmadi, J. E. Shield, Stephen Ducharme, and X. Hong, Assembly of close-packed ferroelectric polymer nanowires via interface-epitaxy with ReS_2, Adv. Mater. **33**, 2100214 (2021).

[34] S. Bertolazzi, P. Bondavalli, S. Roche, T. San, S. Y. Choi, L. Colombo, F. Bonaccorso, and P. Samorì, Nonvolatile memories based on graphene and related 2D materials, Adv. Mater. **31**, 1806663 (2019).

[35] P. E. Blöchl, Projector augmented-wave method, Phys. Rev. B **50**, 17953 (1994).

[36] G. Kresse and D. Joubert, From ultrasoft pseudopotentials to the projector augmented-wave method, Phys. Rev. B **59**, 1758 (1999).

[37] J. P. Perdew, K. Burke, and M. Ernzerhof, Generalized Gradient Approximation made Simple, Phys. Rev. Lett. **77**, 3865 (1996).

[38] S. Grimme, J. Antony, S. Ehrlich, and H. Krieg, A consistent and accurate ab initio parametrization of density functional dispersion correction (DFT-D) for the 94 elements H-Pu, J. Chem. Phys. **132**, 154104 (2010).

[39] S.-i. Takagi, A. Toriumi, M. Iwase, and H. Tango, On the universality of inversion layer mobility in Si MOSFET's: Part I-effects of substrate impurity concentration, IEEE Trans. Electron Devices **41**, 2357 (1994).

[40] S.-i. Takagi, A. Toriumi, M. Iwase, and H. Tango, On the universality of inversion layer mobility in Si MOSFET's: Part II-effects of surface orientation, IEEE Trans. Electron Devices **41**, 2363 (1994).

[41] S. Poncé, W. Li, S. Reichardt, and F. Giustino, First-principles calculations of charge carrier mobility and conductivity in bulk semiconductors and two-dimensional materials, Rep. Prog. Phys. **83**, 036501 (2020).

[42] C.-H. Park, Y.-W. Son, L. Yang, M. L. Cohen, and S. G. Louie, Electron beam supercollimation in graphene superlattices, Nano Lett. **8**, 2920 (2008).